remote sensing

MDPI

Article

Sensitivity Analysis and Optimization of a Radiative Transfer Numerical Model for Turbid Lake Water

JongCheol Pyo [1], Yong Sung Kwon [2], Jae-Hyun Ahn [3], Sang-Soo Baek [4], Yong-Hwan Kwon [5] and Kyung Hwa Cho [4,*]

1 Center for Environmental Data Strategy, Korea Environment Institute, Sejong 30147, Korea; jcpyo@kei.re.kr
2 Environmental Impact Assessment Team, Division of Ecological Assessment, National Institute of Ecology, Seocheon 33657, Korea; wiskys@nie.re.kr
3 Korea Ocean Satellite Center, Korea Institute of Ocean Science and Technology, Busan 49111, Korea; brtnt@kiost.ac.kr
4 School of Urban and Environmental Engineering, Ulsan National Institute of Science and Technology, Ulsan 689-798, Korea; kbcqr@naver.com
5 Electronics and Telecommunication Research Institute, 218 Gajeong-ro, Yeseong-gu, Daejeon 305-700, Korea; yhkwon@etri.re.kr
* Correspondence: khcho@unist.ac.kr; Tel.: +82-52-217-2829

Abstract: Remote sensing can detect and map algal blooms. The HydroLight (Sequoia Scientific Inc., Bellevue, Washington, DC, USA) model generates the reflectance profiles of various water bodies. However, the influence of model parameters has rarely been investigated for inland water. Moreover, the simulation time of the HydroLight model increases as the amount of input data increases, which limits the practicality of the HydroLight model. This study developed a graphical user interface (GUI) software for the sensitivity analysis of the HydroLight model through multiple executions. The GUI software stably performed parameter sensitivity analysis and substantially reduced the simulation time by up to 92%. The GUI software results for lake water show that the backscattering ratio was the most important parameter for estimating vertical reflectance profiles. Based on the sensitivity analysis results, parameter calibration of the HydroLight model was performed. The reflectance profiles obtained using the optimized parameters agreed with observed profiles, with R^2 values of over 0.98. Thus, a strong relationship between the backscattering coefficient and the observed cyanobacteria genera cells was identified.

Keywords: HydroLight; graphical user interface; sensitivity analysis; lake water; reflectance vertical profile

Citation: Pyo, J.C.; Kwon, Y.S.; Ahn, J.-H.; Baek, S.-S.; Kwon, Y.-H.; Cho, K.H. Sensitivity Analysis and Optimization of a Radiative Transfer Numerical Model for Turbid Lake Water. *Remote Sens.* **2021**, *13*, 709. https://doi.org/10.3390/rs13040709

Academic Editor: Hideki Kobayashi
Received: 31 December 2020
Accepted: 11 February 2021
Published: 15 February 2021

1. Introduction

Recently, remote sensing has become a prevalent technique for detecting the dynamics of harmful algae magnitude and timing through the analysis of the optical features of water bodies [1–3]. The optical features of inland water have significant variables such as absorption, scattering, and fluorescence emission that are crucial in identifying the concentration and spatial distribution of algae [4,5]. Furthermore, vertical profiles of the optical information enable the identification of the algal profile at each water depth because harmful species, such as cyanobacteria, can vertically migrate using a buoyancy mechanism to ensure optimal nutrient and light availability [6]. Thus, the optical profile of the water bodies can provide insights on water quality issues, including the detection of harmful algae and water resource management.

The HydroLight model (referred to as HydroLight) is a radiative transfer numerical model that computes the radiance, irradiance, reflectance, and attenuation that are induced by water absorption and scattering [7]. In particular, HydroLight can generate the reflectance spectra as a function of water depth. Several studies have applied this model to estimate water surface reflectance [8,9] and vertical profiles [10,11].

These studies utilized the simulated reflectance to estimate chlorophyll-a concentration, which is an indicator of algal biomass [12]. HydroLight was developed for optical oceanography; therefore, its model parameters describe optical properties of oceans [13]. Furthermore, evidence from recent years has shown that the application of HydroLight can be extended to estuaries, deltaic water bodies, wetlands, rivers, and lakes [14–17]. By extension, further exploration of the model parameters for inland water optics is needed. The identification of the parameter sensitivity determines the importance of model parameters that are highly correlated with the model output and reduces the simulation uncertainty by excluding insignificant parameters.

Sensitivity analysis of the model parameters can provide the most influential parameters [18]. In addition, parameter sensitivity analysis delivers the prerequisite information for model calibration by narrowing the range of parameter selections [19]. The values of the parameters of HydroLight vary for seawater and fresh water because the model parameters are dependent on the absorption and scattering features of the constituents in each water type. The optimal parameters for ocean water may be insensitive to the optical features of inland water [13,20]. Thus, a sensitivity analysis of the parameters of HydroLight needs to be performed to investigate the parameters associated with inland water and to increase the efficiency of the model calibration process. Moreover, sensitivity analysis is carried out by generating an input parameter matrix using a random sampling method, conducting a model simulation, and evaluating the influence and significance of input and output relationships [21]. This process produces numerous model inputs. However, HydroLight implements the simulation based on each observation point; consequently, point-based HydroLight simulation for sensitivity analysis can be exceedingly time-consuming.

Therefore, this study was to develop a sensitivity analysis tool for HydroLight; the proposed tool can implement multi-point simulations. Parameter calibration was conducted to identify the optimal values of the parameters that are highly sensitive to the optical features of inland water. To achieve these objectives, this study (1) designed a MATLAB GUI structure, (2) built the GUI configuration for sensitivity analysis with multiple executions of HydroLight, (3) implemented the parameter sensitivity analysis for the vertical reflectance in the lake, and (4) optimized the HydroLight parameters for evaluating the reflectance spectra at the surface and beneath the surface of the lake water, in addition to depths of 0.5 m and 1.0 m.

2. Materials and Methods

2.1. Study Area

Figure 1 shows the study area, which is in Daecheong dam (36°28′40.7″ N, 127°28′51.3″ E). The water from the dam is mainly utilized for domestic water supply. The dam has a surface area of 72.8 km^2, a storage volume of 1490 $\times$ 10^6 m^3 and a length of 86 km. The average water depth is 20 m. In the Daecheong dam region, the Chuso (CS) and Huinam (HN) regions, denoted by the red boxes in Figure 1, were selected for the case study. In particular, CS has been reported as a region with severe cyanobacteria outbreaks because of a high nutrient load and prolonged water retention time [22]. HN has a deeper water depth (i.e., 25 m) and a shorter water retention time compared to CS, resulting in relatively fewer algal blooms. [23].

2.2. Observation Data and Model Setup

This study conducted field monitoring in the regions of HN and CS in 2018 and 2019. Tables A1 and A2 present the specific sampling periods and observed data points. The monitoring was conducted under clear sky conditions with a light wind speed of less than 5 m s^{-1}. At each point, the radiance from the water surface and irradiance from the sky were measured using an ASD hand-held VNIR spectroradiometer device with specific accessories, including bare fiber with the cosine irradiance collector (Malvern Panalytical Ltd., Malvern, UK). The measurement protocol maintained an azimuth angle between 130°

and 135° and a viewing angle between 35° and 40° [7]. Based on the measured radiance and irradiance, the remote sensing reflectance of the water surface was calculated as

$$R_{rs}(\lambda) = \frac{L^t_w(\lambda) - cL_{sky}(\lambda)}{E_d(\lambda)} \quad (1)$$

where λ is the spectral wavelength; $R_{rs}(\lambda)$ is the remote sensing reflectance at the water surface; $L^t{}_w(\lambda)$ the total radiance from the water including sky radiance reflected at the air-water interface (W m^{-2} nm^{-1} sr^{-1}); $L_{sky}(\lambda)$ is the radiance from the sky (W m^{-2} nm^{-1} sr^{-1}); c is defined as 0.025 implying a Fresnel reflectance ratio for the skylight; and $E_d(\lambda)$ is the downwelling irradiance at the water surface (W m^{-2} nm^{-1}).

The radiance of water was vertically measured, at the subsurface and at depths of 0.5 m and 1.0 m, by using an attachable jumper optical fiber with a length of 1.5 m. The observed reflectance at each depth was calculated using Equation (6). In addition, an EXO-2 multiparameter water quality instrument (YSI Inc., Yellow Springs, Ohio, USA) was employed to measure the vertical profiles of the chlorophyll-a (Chl-a) and total suspended solids (TSS) concentrations. Water samples were also collected for the absorption analysis of Chl-a. The detailed experimental procedure is described in [24]. In addition, algal identification and cell counts were analyzed using an optical microscope, in accordance with the standard methods for examining water pollution [25].

The algal cells were used to investigate the relationship between cell characteristics and the optical scattering of water.

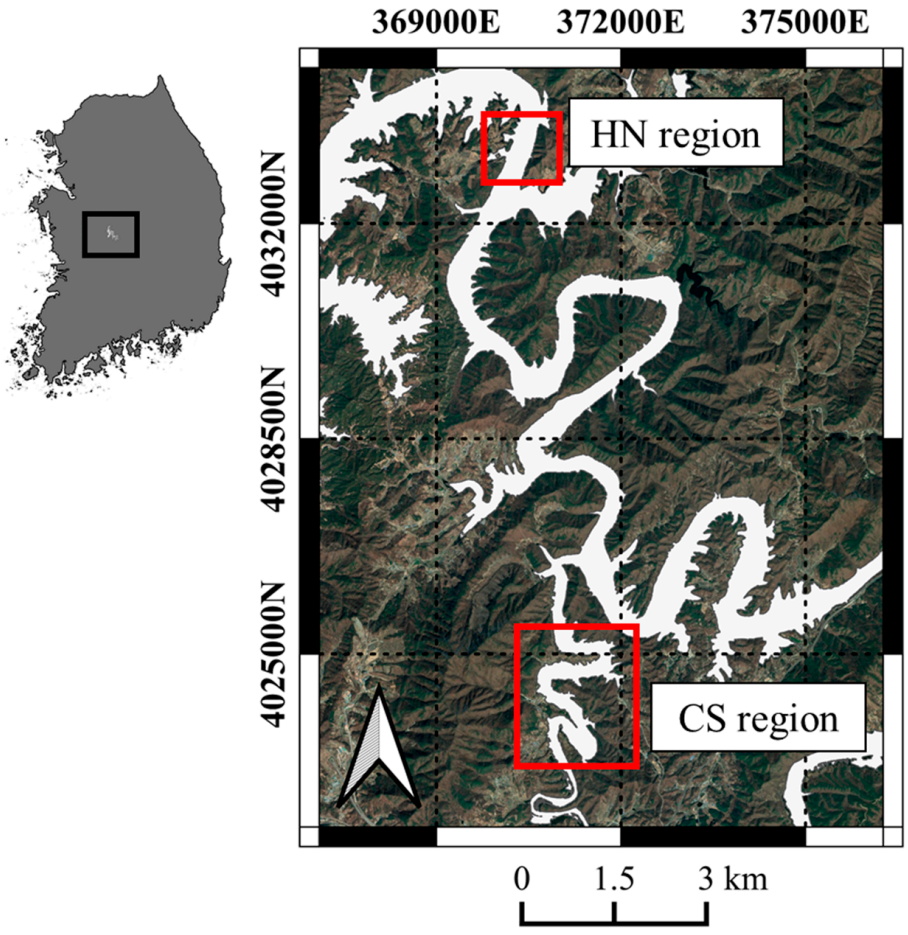

Figure 1. Case study area in the Daecheong dam; the labels "HN region" and "CS region" and the adjacent red boxes indicate the Huinam and Chuso regions, respectively.

2.3. Radiative Transfer Numerical Model: HydroLight

This study simulated the reflectance profile of lake water using the radiative transfer numerical model HydroLight version 5.2 (Sequoia Scientific Inc., Bellevue, Washington, DC, USA) [26]. HydroLight is an algorithm for solving the radiative transfer equation. The simulation considers chlorophyll fluorescence and Raman scattering by water. Water surface condition was determined by the clear sky having a sun zenith angle of 30° and no waves. The water depth was set as infinite. The condition of inherent optical properties (IOPs) was used by the observed absorption coefficient of phytoplankton. In addition, HydroLight used the vertical chlorophyll-a (Chl-a) and total suspended solids (TSSs) profiles, which were observed using the EXO-2 sensor for calculating the absorption and scattering coefficients as a function of depth. The total absorption of the water constituents was modeled using the following equation:

$$a(z,\lambda) = a_{\mathrm{w}}(\lambda) + a_{\mathrm{chla}}(z,\lambda) + a_{\mathrm{p}}(z,\lambda) + a_{\mathrm{cdom}}(z,\lambda), \quad (2)$$

where $a(z,\ \lambda)$ is the total absorption coefficient of water constituents (m^{-1}) at depth z (m); $a_{\mathrm{w}}(\lambda)$ is the absorption coefficient of pure water; $a_{\mathrm{chla}}(z,\lambda)$ is the absorption coefficient of chlorophyll-a; $a_{\mathrm{p}}(z,\ \lambda)$ is the absorption coefficient of particulate matter except for the algal pigment (m^{-1}); and $a_{\mathrm{cdom}}(z,\ \lambda)$ is the absorption coefficient of colored dissolved organic matter (CDOM) (m^{-1}). This study used the observed absorption coefficient for $a_{\mathrm{p}}(z,\ \lambda)$ to calculate the total absorption coefficient [7]. However, CDOM absorption is calculated using an exponentially decaying function that covaries with Chl-a absorption as

$$a_{\mathrm{cdom}}(z,\lambda) = p_0 a_{\mathrm{chl}}(z,440)\exp[-q_0(\lambda - 440)], \quad (3)$$

where $a_{\mathrm{chl}}(z,440)$ is the absorption coefficient of Chl-a for the wavelength of 440 nm (m^{-1}) at depth z (m); 440 nm is the reference wavelength; p_0 is the empirical parameter; and q_0 is the decay constant.

In addition, the total scattering coefficient is modeled via the following equation:

$$b(z,\lambda) = b_{\mathrm{w}}(\lambda) + b_{\mathrm{p}}(z,\lambda) \quad (4)$$

Here, $b(z,\lambda)$ is the scattering coefficient of water constituents (m^{-1}) at depth z (m); $b_{\mathrm{w}}(\lambda)$ is the scattering coefficient of lake water (m^{-1}); and $b_{\mathrm{p}}(z,\lambda)$ is the scattering coefficient of the particulate matters (m^{-1}).

The scattering coefficient of the particulate matter follows a power law referred by [27] as

$$b_{\mathrm{p,x}}(z,\lambda) = b_0\left(\frac{550}{\lambda}\right)^m [\mathrm{x}(z)]^n, \quad (5)$$

where x indicates the particulate matter, including Chl-a and TSS; $b_{\mathrm{p,x}}(z,\lambda)$ is the scattering coefficient of Chl-a and TSS (m^{-1}) at depth z (m); x(z) is the concentration of Chl-a and TSS (mg m^{-3}) at depth z; 550 nm is the reference wavelength; and b_0, m, and n are model parameters. For the scattering phase function, the backscattering ratios ($b_{\mathrm{pb}}/b_{\mathrm{p}}$) of Chl-a and TSS were set to a constant at each depth.

Based on the IOPs, HydroLight solves the radiative transfer equation to generate the radiance at each depth [7]. The remote sensing reflectance is then calculated via the ratio of water radiance and downwelling irradiance as follows:

$$r_{\mathrm{rs}}(z,\lambda) = \frac{L_{\mathrm{u}}(z,\ \lambda)}{E_{\mathrm{d}}(z,\ \lambda)} \quad (6)$$

where $r_{\mathrm{rs}}(z,\lambda)$ is the remote sensing reflectance (sr^{-1}) at depth z (m); $L_{\mathrm{u}}(z,\ \lambda)$ is the upwelling radiance (W m^{-2} nm^{-1} sr^{-1}); and $E_{\mathrm{d}}(z,\lambda)$ is the downwelling irradiance (W m^{-2} nm^{-1}).

2.4. Sensitivity Analysis

For sensitivity analysis, the parameter set generation is performed using the Latin hypercube (LH) and one-factor-at-a-time (OAT) sampling methods. LH sampling is one of the most sophisticated random sampling methods; it is based on the Monte Carlo method [28]. The LH sampling method subdivides the distribution of each parameter into N ranges, after which one parameter value is randomly sampled.

Then, OAT sampling is carried out by changing one parameter value at a time while the other parameter values are fixed [29,30]. Thus, the LH-OAT method produces N × (P+1) number of input files, where P is the number of the selected parameters for sensitivity analysis [19,31,32].

After N × (P+1) model simulations, the elementary effect (EE) method is employed to implement the sensitivity analysis of each input parameter by ranking the parameters in order of importance [30,33]. The EE value is calculated by the differentiation of the model output with respect to the input parameter as

$$\mathrm{EE}_i(p) = \frac{\mathrm{f}(p_1, \ldots, p_i + \Delta, \ldots, p_k) - \mathrm{f}(p)}{\Delta} \tag{7}$$

where p_i is the ith input parameter of the model; Δ is the predetermined perturbation factor of p_i; f(p) is the model output for parameter p; and f($p_1, \ldots, p_i+\Delta, \ldots, p_k$) is the model output for the change Δ in p_i.

The finite distribution of EE values can provide sensitivity indices using the mean and standard deviation of the EEs as follows:

$$\mu = \frac{\sum_{i=1}^{N} \mathrm{EE}_i}{N} \tag{8}$$

$$\sigma = \sqrt{\frac{1}{N} \sum_{i=1}^{N} (\mathrm{EE}_i - \mu)} \tag{9}$$

where μ is the mean of EEs; σ is the standard deviation of EEs and N is the number of parameters.

The mean of the EEs indicates the sensitivity strength with regard to parameter change and model output response [34]. A high EE means implies that the output has a high sensitivity to the parameter. Furthermore, the standard deviation of the EEs represents the strength of interaction of a particular parameter with other parameters [35]. In this study, the EE method for sensitivity analysis was implemented using the SAFE Toolbox of MATLAB software version 2019a (MathWorks Inc., Natick, MA, USA) [36].

In the CS region, a total of 104 monitoring and experimental data points were utilized as input data for HydroLight model simulation. This study selected 12 parameters for sensitivity analysis. The number of OAT sampling points was assigned as 10, thereby generating a total of 2,990 input files (i.e., (10 × (12+1)) × 23) for HN and a total of 13,520 inputs (i.e., (10 × (12+1)) × 104) for CS. In addition to the parameters in Equations (2)–(5), the backscattering ratio for Chl-a and TSS, Chl-a fluorescence quantum efficiency, and Raman scattering coefficient of water were chosen for analysis because the concentrations of the constituents of the lake water are relatively high compared to those of the constituents of ocean water. Before conducting sensitivity analysis, the ranges of the selected parameters were defined based on previous studies that mainly focused on investigating the optical properties of inland waters (Table 1).

2.5. GUI Development for Sensitivity Analysis of HydroLight

In this study, the GUI structure for sensitivity analysis of HydroLight parameters was developed using MATLAB. The GUI performed input file generation based on LH–OAT sampling; furthermore, it carried out multi-point HydroLight simulation by establishing a multiple execution system. Figure 2 presents a schematic of the GUI-based HydroLight

sensitivity analysis program. First, an input template and parameter information (including name and specific range of the selected parameters) are loaded on to the model (Figures 2a and 3a). The formats of the input template and the parameter information are text and excel files, respectively. After loading the files, the number of parameters, P, is displayed on the GUI (Figure 3). Subsequently, LH–OAT sampling of the model parameters is carried out (Figures 2b and 3b). The number of sampling points, N, is determined by the user, and then the sampling process generates N × (P+1) parameter sets that are displayed by GUI. Furthermore, a set of observation data is imported, after which N × (P+1) input files are generated, as shown in Figures 2c and 3c.

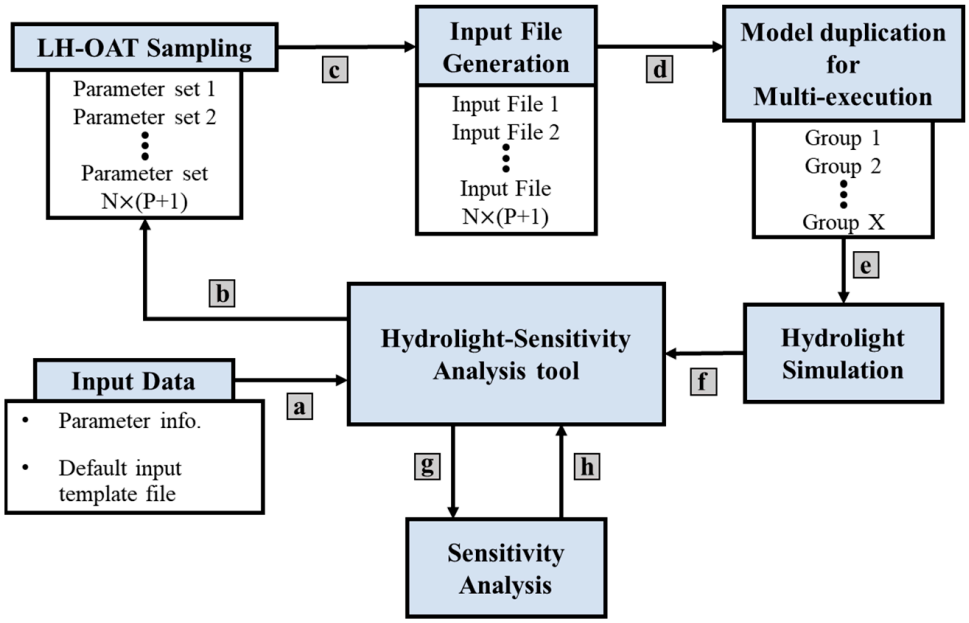

Figure 2. Schematic for program workflow—(**a**) is a model parameter and input template load; (**b**) is the Latin hypercube and one-factor-at-a-time (LH–OAT) sampling implementation for the parameters; (**c**) is the total input generated based on observation data and LH–OAT sampling results; (**d**) is the preparation for multiple executions by duplicating the model set as a group; (**e**) is the multi-point HydroLight simulation; (**f**) is the load of the simulated reflectance profile; (**g**) is the implementation of parameter sensitivity analysis by comparing simulated reflectance with direct observation; and (**h**) is the display of the sensitivity analysis result.

All of the input files are prepared by multiplying the total number of observation points N × (P+1) by the number of input files (Figure 3). After input file generation is completed, the model is replicated based on the number of multi-executions, X (Figures 2d and 3d). Then, multi-point simulations are simultaneously performed upon pressing the model simulation button (Figures 2e and 3e). Furthermore, the simulation results are gathered for sensitivity analysis (Figures 2f and 3f). The model error is determined based on the difference between the modeled reflectance profiles and observed profiles; the errors are then transferred to the sensitivity analysis toolbox (Figures 2g and 3g). Finally, the sensitivity analysis results of each parameter are computed via the mean and standard deviation of the EEs, and the results are shown in the result window and as a scatter plot (Figures 2h and 3h).

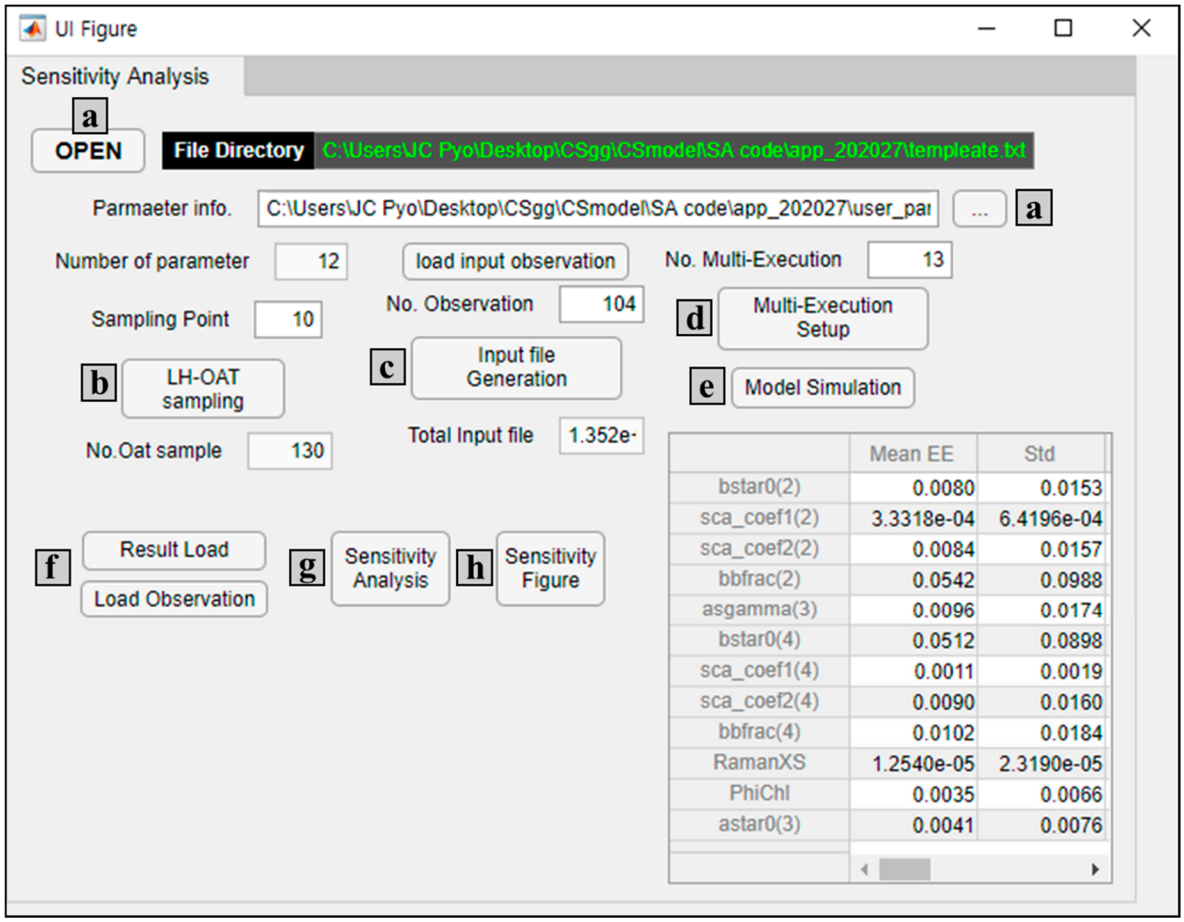

Figure 3. Graphical user interface (GUI) design of HydroLight sensitivity analysis program—(**a**) is the implementation button of the loading template for the HydroLight input file and the selected parameter for sensitivity analysis; (**b**) is the switch for implementing the LH–OAT sampling based on the parameters and user-defined sampling points; (**c**) is the button for generating the total number of input files; (**d**) is the button for generating multiple simulation sets; (**e**) is the multiple execution button of the HydroLight simulation; (**f**) is the buttons for loading simulated reflectance results and corresponding observation results; and (**g**,**h**) are the switches for conducting parameter sensitivity analysis and visualizing the sensitivity analysis results, respectively.

2.6. Parameter Optimization

Once the important parameters were identified, the selected parameters were calibrated to calculate the reflectance profiles of lake water. A pattern search algorithm was adopted to calibrate the model parameters. Pattern search is one of the numerical optimization methods without the gradient of the optimization equation [37]. Furthermore, this method is simple and efficient to optimize diverse objective functions because it is based on direct function evaluations without the derivatives. Thus, this method can be employed for parameter optimization of the HydroLight model. In addition, pattern search is capable of convergence to local minima by identifying the neighbor parameters of the current point and then investigating an optimal direction. If all neighboring points cannot find a decrease in the error, thereby reducing the search step. Thus, the search of minimizing the error stops when the step is substantially small that converges to the local minimum. In addition, manual calibration was also performed to improve the results of the pattern search implementation [38].

Table 1. Parameter information for sensitivity analysis.

Component	Parameter of HydroLight	Min	Max	Reference
Chlorophyll-a	Scattering coefficient (b_0)	0.1	1.0	
	Scattering coefficient (m)	0	1.0	
	Scattering coefficient (n)	0	1.0	[39]
	Backscattering ratio	0.0005	0.021	[40]
	Chlorophyll-a fluorescence efficiency	0.003	0.02	[41]
CDOM	Empirical parameter (p_0)	0.2	1.0	[42]
	Exponential decay constant (q_0)	0.012	0.021	
TSS	Scattering coefficient (b_0)	0.1	1.0	
	Scattering coefficient (m)	0	1.0	
	Scattering coefficient (n)	0	1.0	[39]
	Backscattering ratio	0.0005	0.021	[43]
Water	Raman scattering coefficient	0.000232	0.00032	[44]

3. Results and Discussions

3.1. Vertical Profile of Chl-a and TSS

Tables A1 and A2 show the Chl-a and TSS concentrations in HN and CS at the surface, subsurface, and at depths of 0.5 m and 1.0 m. These specific depths corresponded to the depths at which remote sensing can measure reflectance. The EXO-2 sensor can measure the vertical profiles of water constituents, including Chl-a and phycocyanin, and the turbidity; furthermore, the measured profiles show good agreement with experimentally analyzed concentrations of water quality variables [45–48]. In 2018 and 2019, CS showed higher Chl-a and TSS concentrations at each depth than the concentrations in HN. This was due to the river-bends in CS, where the water retention time is high. In particular, CS exhibited a high Chl-a concentration in July, August, and early September. A high water temperature and low flow velocity triggered the increase of algal growth. Furthermore, the variation of the solar radiation intensity may have resulted in the vertical variation in the concentration of Chl-a due to the algal buoyancy mechanism [49]. During the periods with high Chl-a concentrations, high TSS concentrations were also observed in CS. However, when TSS showed the highest concentration level, on 16 August 2018, the concentration of Chl-a was found to be relatively low. This may be because a high TSS concertation reduces the light availability for the phytoplankton owing to increased light attenuation [50].

In HN, the concertation of TSS was generally higher than that of Chl-a, at each depth. Thus, based on the observed concentrations of the constituents, the optical properties may differ for the water in CS and HN, resulting in different parameter sensitivities for the HydroLight model.

3.2. Sensitivity Analysis

A sensitivity analysis tool for the HydroLight model was implemented to determine the influential optical parameters for HN and CS. Figure 4 shows the sensitivity analysis results for HN. The major parameters were related to suspended solids. Notably, the backscattering ratio for suspended solids was the most sensitive parameter in the case of HN, whereas the scattering coefficient (n) was secondary. In Table 2, the parameters are ranked based on the sensitivity, with respect to the depth (surface level, subsurface level, 0.5 m, and 1.0 m). The parameter ranking at each depth was observed to possess a similar ranking because the reflectance profile was calculated as a function of depth [7]. Figure 5 presents the sensitivity analysis results for CS, showing that the highly sensitive parameters were associated with Chl-a. The backscattering ratio of Chl-a was the most sensitive parameter, and the specific scattering coefficient (b_0) of suspended solids was secondary in the case of CS. The sensitivity ranking of the parameters showed a similar trend with regard to the depth profiles (Table 2). The difference in the optical features of the HN and CS regions may induce different parameter sensitivity results. HN exhibited

a low Chl-a concentration; thus, the effect of the parameters related to non-algal matter was strong for HN. However, CS primarily contained a high concentration of Chl-a and suspended solids, resulting in the most sensitive parameters being related to both Chl-a and TSS.

The most sensitive parameter, namely, the backscattering ratio, is considered a critical factor for addressing discrepancies between modeling-based and observed remote sensing data because this ratio is indicative of the particle composition in water bodies. [51]. In particular, this ratio is related to the level of suspended solids and dissolved matter in fresh water, which significantly influences the reflectance. In addition, the backscattering ratio was used to estimate the bulk refractive index with respect to the particle size distribution [52].

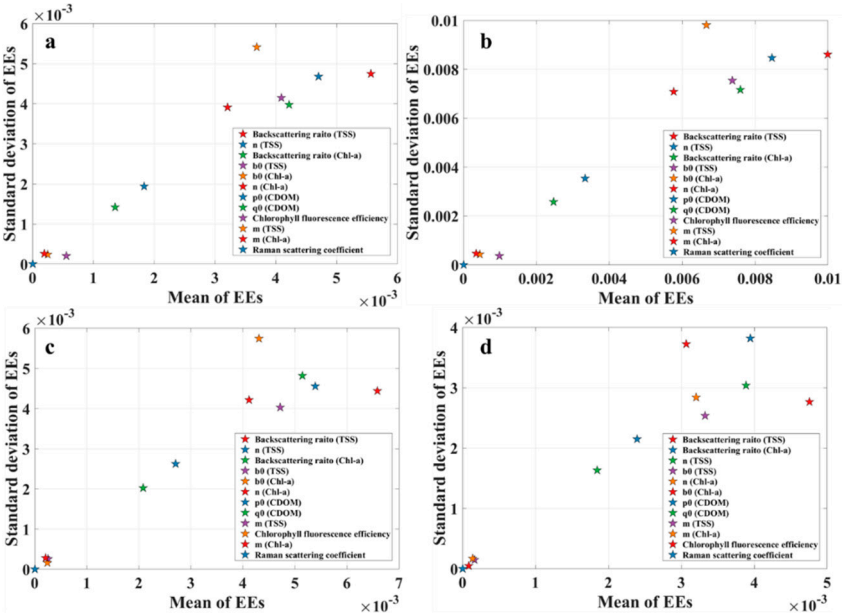

Figure 4. Sensitivity analysis results for the HN region—(**a**) is the parameter sensitivity result at the water surface level; EE indicates the elemental effect values calculated by the model output differences from the parameter change; (**b**) is the sensitivity result at the subsurface; (**c**) is the sensitivity result at a depth of 0.5 m; and (**d**) is the sensitivity results at a depth of 1.0 m.

Table 2. Sensitivity parameter ranking.

		HN				CS			
Component	**Parameters**	**0(+)**	**0(−)**	**0.5m**	**1.0m**	**0(+)**	**0(−)**	**0.5m**	**1.0m**
Chlorophyll-a	Scattering coefficient (b_0)	5	5	5	6	4	4	5	5
	Scattering coefficient (m)	11	11	11	10	11	10	11	11
	Scattering coefficient (n)	6	6	6	5	3	3	3	3
	Backscattering ratio	3	3	3	2	1	1	1	1
	Chlorophyll-a fluorescence efficiency	9	9	10	11	9	9	9	9
CDOM	Empirical parameter (p_0)	7	7	7	7	7	7	7	7
	Exponential decay constant (q_0)	8	8	8	8	8	8	8	8
TSS	Scattering coefficient (b_0)	4	4	4	4	2	2	2	2
	Scattering coefficient (m)	10	10	9	9	10	11	10	10
	Scattering coefficient (n)	2	2	2	3	6	6	6	6
	Backscattering ratio	1	1	1	1	5	5	4	4
Water	Raman scattering coefficient	12	12	12	12	12	12	12	12

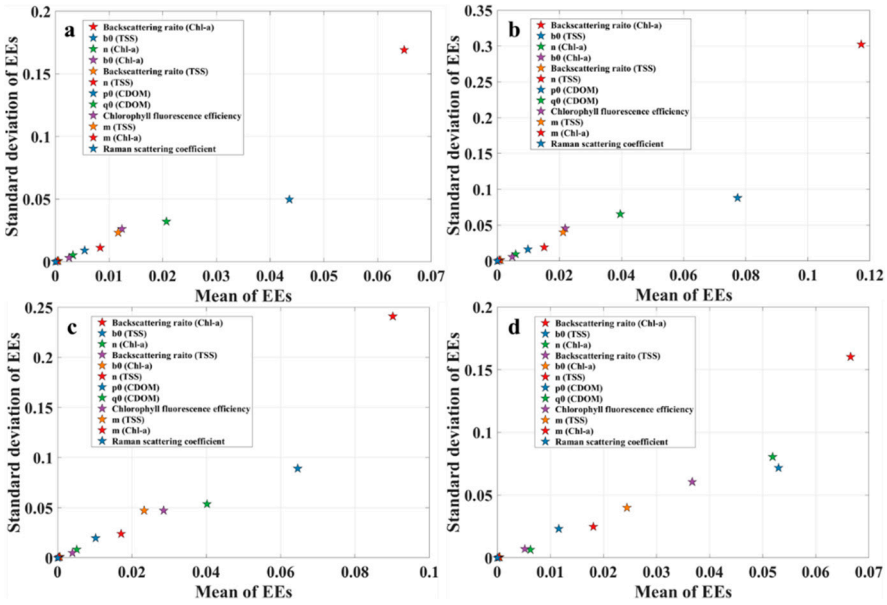

Figure 5. Sensitivity analysis results for the CS region—(**a**) is the parameter sensitivity result at the level of surface water; (**b**) is the sensitivity result at the subsurface; (**c**) is the sensitivity result at a depth of 0.5 m; and (**d**) is the sensitivity result at depth of 1.0 m.

This indicates that the sensitivity of the ratio depended on the concentration of Chl-a or TSS due to their various refraction indexes [53]. Furthermore, this ratio was utilized as a proxy to determine the scattering phase function that was used to fit the light field of the water column [26]. In addition to the backscattering ratio, the scattering coefficients (i.e., n and b_0) showed secondary importance in estimating reflectance by calculating the backscattering coefficient because these parameters directly affected the concentrations of Chl-a and TSS, as seen in Equation (5) [54]. However, the scattering coefficient (m) was used to assign the wavelength, a parameter with minor sensitivity, for both Chl-a and TSS. The wavelength variation, with respect to the reference wavelength, insignificantly affected the reflectance profile. Prior studies normally used previously published values of this parameter.

CDOM affected the intrinsic properties of water, such as Chl-a absorption level, because the optical features of CDOM substantially affect the photo-processes and radiance in the upper water column. However, the parameters (p_0 and q_0) for CDOM showed low sensitivity to the reflectance profile in both HN and CS (Table 2). The CDOM exhibited relatively low absorption compared to the other constituents, and the optical feature corresponding to CDOM is negligible in the red spectral band because CDOM absorption exponentially decreases with an increase in wavelength [55]. Particularly, several studies have investigated the spectral slope, q_0, for fitting the CDOM absorption curve because the slope values were site-specific and varied with the water constituents [42,56–58].

Chl-a fluorescence quantum efficiency was the 11th (of 12) parameter in terms of sensitivity. This parameter affected specific Chl-a absorption and also improved the fit of the Chl-a reflectance estimates with the near-infrared spectral peaks [59,60]. However, the fluorescence quantum efficiency has been considered less variable than is commonly believed [61]. That is, the fluorescence efficiency value is generally constant across a wide range, although the variation of the fluorescence efficiency is certainly valuable for particular species or conditions [62].

The extent of the Raman scattering was the least sensitive parameter in this study. That is, the effect of the variability of Raman scattering of water was relatively insignificant when calculating the vertical reflectance of fresh water. This is in accordance with the authors of [63], who also found a lack of significant differences in Raman scattering between clear ocean water and pure water.

3.3. Parameter Calibration for Reflectance Profile

After implementing the sensitivity analysis tool for the HydroLight model, this study calibrated the selected parameters for sensitivity analysis in order to estimate the reflectance profile in terms of the six examples in Figure 6. The value of the downwelling diffuse attenuation coefficient indicated that the depth of penetration of sunlight into water varied from 0.69 m to 2.17 m, which was calculated by 1/Kd(490) [63]. The penetration depths were less than 1.0 m in July and August, but over 2.0 m in October, because the penetration depth of the turbid lake water was significantly affected by the absorption and scattering effect arising from suspended particulate matter [64].

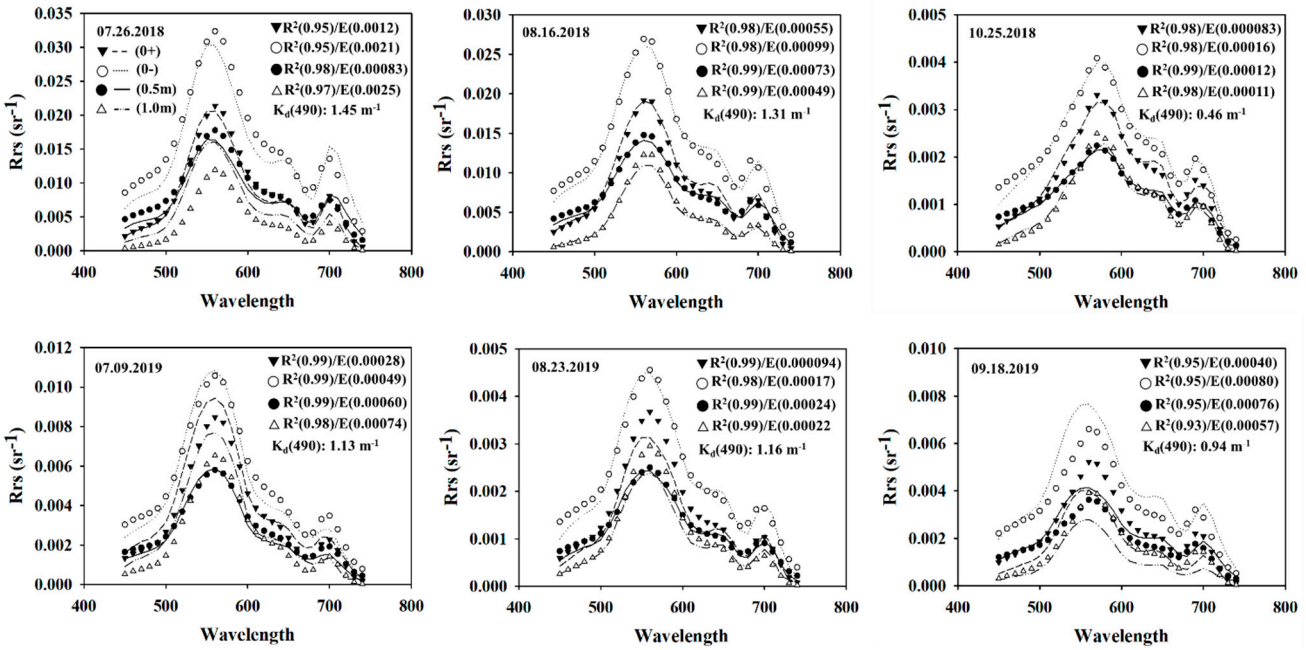

Figure 6. Remote sensing reflectance simulations using the calibrated parameters for the example sampling points. The dotted, dashed, solid, and double dotted lines represent the observed reflectance profiles with respect to the surface, beneath of surface, 0.5 m, and 1.0 m; black inverted triangles indicate the surface reflectance simulated using HydroLight; white circles represent the subsurface reflectance; black circles indicate the reflectance at 0.5 m of water depth; and white triangles represent the reflectance at 1.0 m. E indicates the root mean square error (sr^{-1}). $K_d(490)$ is the downwelling diffuse attenuation coefficient at 490 nm.

Shen et al. [65] observed the effect of variation of the penetration depth from 0.09 m to 1.36 m in lake waters with high concentrations of chlorophyll-a and suspended particulate matters. The simulated vertical profiles of reflectance showed good agreement with the observed profiles. The simulated spectra at various depths (i.e., surface, subsurface, 0.5 m, and 1.0 m) had R^2 values > 0.93 and RMSE values < 0.0025 sr^{-1}. Lee at al. [66] showed that subsurface reflectance simulated using the HydroLight model had an error of 0.9%. In Nouchi et al. [67], the reflectance spectra were estimated at a depth of 1.0 m and measured within an acceptable level of uncertainty. However, the simulated spectra in the spectral range of 615 nm to 630 nm showed disagreements with the observed spectra, but the discrepancy was still within the range of the expected observation uncertainty (Figure 6). This may be because of the difficulty of accurately reflecting the characteristics of a cyanobacteria-dominant bloom due to the presence of phycocyanin, which leads to a spectral curvature at 620 nm [6]. Overall, the calibrated parameters of the HydroLight model provided reasonable simulation accuracy for the water reflectance of inland water with respect to the depth.

Table 3 presents the calibrated parameter ranges. The most sensitive parameter, the backscattering ratio, had a wide range. Although the theoretical value of the backscattering

ratio is 0.02, based on oceanography [52], a backscattering ratio lower than 0.02 was also assigned based on observation, reflecting the characteristics of water dominated by phytoplankton and organic detritus [54,68–70]. The increase in the backscattering ratio was induced by a decrease in the size of the suspended particles [71]. Specifically, very small organic and detrital matter, with a size between 1.0 µm and 10.0 µm, mainly contributed to the backscattering coefficient of the water [72,73]. Snyder et al. [69] and Whitmire et al. [54] showed that the backscattering ratio of coastal waters varied between 0.005 and 0.060. McKee and Cunningham [74] showed that the backscattering ratio for the ocean water varied between 0.005 and 0.050. Loisel et al. [68] found that the backscattering ratio of coastal water changed from 0.0024 to 0.0417. Boss et al. [75] showed that the backscattering ratio of seawater varied from 0.005 to 0.035. These backscattering values were relatively high compared to the calibrated backscattering ratio in this study (Table 3). The dynamic range of the backscattering ratio may imply the large variability of the particle composition of inland water with a high concentration of optical matters. Haltrin et al. [76] reported that the backscattering ratio in turbid water increased with the concentration of Chl-a. In our study, the calibrated scattering coefficients (b_0 and n) showed relatively high values compared to those for ocean water (Table 3). The high parameter values lead to the relatively high backscattering coefficients, which in turn corresponded to high Chl-a and TSS concentrations in fresh water [77]. The typical values of b_0 and n for ocean water were documented as 0.30 and 0.62, respectively [27,78]. In the case of turbid inland water, the parameters needed to be adjusted because the backscattering coefficient could not be elucidated using the parameters published based on oceanography [43]. Conversely, the scattering parameter (n) was corroborated with the value in the literature as 1.0 [27].

Table 3. Calibrated parameters for estimating reflectance profile.

Component	Parameters	Optimized Parameter Range
Chlorophyll-a	Scattering coefficient (b_0)	0.4–0.8
	Scattering coefficient (m)	1.0
	Scattering coefficient (n)	0.5–0.9
	Backscattering ratio	0.0009–0.01
	Chlorophyll-a fluorescence efficiency	0.002–0.018
CDOM	Empirical parameter (p_0)	0.6–0.7
	Exponential decay constant(q_0)	0.020
TSS	Scattering coefficient (b_0)	0.3–0.8
	Scattering coefficient (m)	1.0
	Scattering coefficient (n)	0.4–0.9
	Backscattering ratio	0.0008–0.01
Water	Raman scattering coefficient	0.00026

The calibrated p_0 for CDOM showed a higher value than 0.20, which is the typical value for coastal waters (Table 3). This may be due to the relatively high concentration of CDOM in inland water compared to that in ocean water. However, the calibrated decay constant, q_0 was found to have a similar value to that obtained in previous studies. Green and Blough [79] documented that the decay constant value for seawater ranged from 0.019 to 0.021. Stedmon and Markager [80] suggested a decay constant value of 0.0194 for coastal water. Schwarz et al. [57] showed that the decay constant was 0.0173 for global ocean water. Thus, this study found that there was no significant difference in the decay constant values between ocean water and inland water.

The Chl-a fluorescence quantum efficiency exhibited a wide range for the calibrated value, which was lower than the typical value of 0.02 (Table 3). Gilerson et al. [62] also reported that the Chl-a fluorescence efficiency varied from 0.005 to 0.01. The Chl-a fluorescence efficiency was directly influenced by the concentration of the water constituents. The value of the Chl-a fluorescence efficiency decreases as TSS concentrations increase because of decreasing light availability due to the strong light attenuation [61].

Regarding the least sensitive parameter, the Raman scattering coefficient of water, there was no significant difference between sea and fresh water. The calibrated Raman scattering coefficient of water showed the same value as that for coastal water [26] (Table 3).

3.4. Scattering Property for Cyanobacteria Genera Cells

After calculating the remote sensing reflectance, the inherent optical backscattering coefficient was utilized to deduce the optical properties of water quality constituents such as algal cells and particulate organic carbon matter [69]. In this study, the absorption coefficients of phytoplankton were measured experimentally, which were then used to simulate the reflectance spectra derived from the HydroLight model. As evidenced by the calculated reflectance, the reflectance simulation was accurate and provided reasonable values for the backscattering coefficients, thereby approximating the relationship between the coefficients and the dominant algal cells. Figure 7 presents the simulated backscattering spectra at the subsurface of water. These spectra decrease exponentially with an increase in the wavelength (Figure 7a,c). Furthermore, the values of these spectra varied substantially with respect to the sampling points and periods due to the different compositions of the optical matter [81]. In particular, this study focused on variations in the backscattering coefficient in response to a change in the number of cyanobacteria cells, because the study area experiences frequent cyanobacteria bloom. The value of the backscattering coefficient was found to increase when the number of cyanobacteria cells increased (Figure 7b,d). [82] reported a logarithmic relationship between the backscattering coefficient and the biomass of *Microcystis*. The high scattering was attributed to the volume, length, and diameter of the cyanobacteria cells [83,84]. In addition, the internal gas vacuoles in cyanobacteria also caused an increase in backscattering due to the increased scattering at backward angles exceeding 90° [85,86]. The specific genus of the cyanobacteria associated with the backscattering coefficient at 550 nm is presented in Figures 8 and 9. The wavelength of 550 nm was chosen considering the strong reflectance peaks of phytoplankton [87]. The backscattering coefficient of 0.1781 m^{-1}, observed on 9 September 2018, was caused by the cyanobacteria cell concentration exceeding 1.9×10^6 cells mL^{-1} (Figure 8c). In particular, *Oscillatoria limnosa* was a dominant species with more than 1.6×10^6 cells mL^{-1}. On the contrary, the backscattering coefficient of 0.0117 m^{-1}, observed on 25 October 2018, was driven by *Microcystis aeruginosa* with 3.6×10^3 cells mL^{-1} (Figure 8d). On 9 July 2019 and 24 July 2019, total cyanobacterial cell concentrations exceeding 2.8×10^4 cells mL^{-1} and 3.4×10^5 cells mL^{-1} induced backscattering coefficients of 0.0422 m^{-1} and 0.1742 m^{-1}, respectively. During these periods, *Aphanizomenon flosaquae* and *Microcystis aeruginosa* were the dominant genera with concentrations exceeding 1.6×10^4 cells mL^{-1} and 1.7×10^5 cells mL^{-1}, respectively (Figure 9a,b). The small size, gas vesicles, heterocyst, and akinetes of *Microcystis* and *Aphanizomenon* genera likely resulted in the high backscattering values [88]. Moore et al. [13] also reported backscattering values between 0.02 m^{-1} and 0.15 m^{-1} at 443 nm for cyanobacteria concentrations ranging from 1×10^4 cells mL^{-1} to 6×10^5 cells mL^{-1}.

3.5. Implication of Developing Sensitivity Analysis Tool

The GUI software provided the sensitivity analysis results for the HydroLight model parameters for inland water. Based on the results, this study calibrated the parameters for calculating the reflectance profile and then interpreted the calibrated parameters for representing the optical properties of fresh water. The GUI software is very straightforward and has obvious advantages. First, the GUI software substantially reduced the HydroLight simulation time. Originally, it took approximately 50 h to simulate 2990 input files for the HN region (i.e., 1 min for each simulation), but with the GUI software, it only took 4 h to simulate the input files using 13 multiple executions. Moreover, the simulation of 13,520 input files for the CS region took approximately 225 h using the normal simulation; in contrast, the simulation time was reduced to approximately 17 h using the GUI software. Second, after the model simulations, the GUI software automatically gathered the simu-

lation results in order to prepare for the sensitivity analysis. Third, the sensitivity results were then provided, and the mean and standard deviation values (Figure 3) and related scatter figures (Figures 4 and 5) were displayed. Therefore, the GUI software developed in this study improves the effectiveness and range of applicability of the HydroLight software with regard to sensitivity analysis. In addition, the versatility of the GUI software allows additional sensitivity analyses to be conducted; furthermore, the software can be consistently employed as new datasets become available for various study areas. Several studies also proved these kinds of advantages in developing GUI software for various objects [89–92]. In the future, a more practical GUI software should be developed by extending the proposed software for studying and estimating water constituents that affect water quality. The software will optimize HydroLight model parameters and then calculate the Chl-a, TSS, CDOM, and phycocyanin concentrations by selecting proper bio-optical algorithms using the simulated reflectance profile.

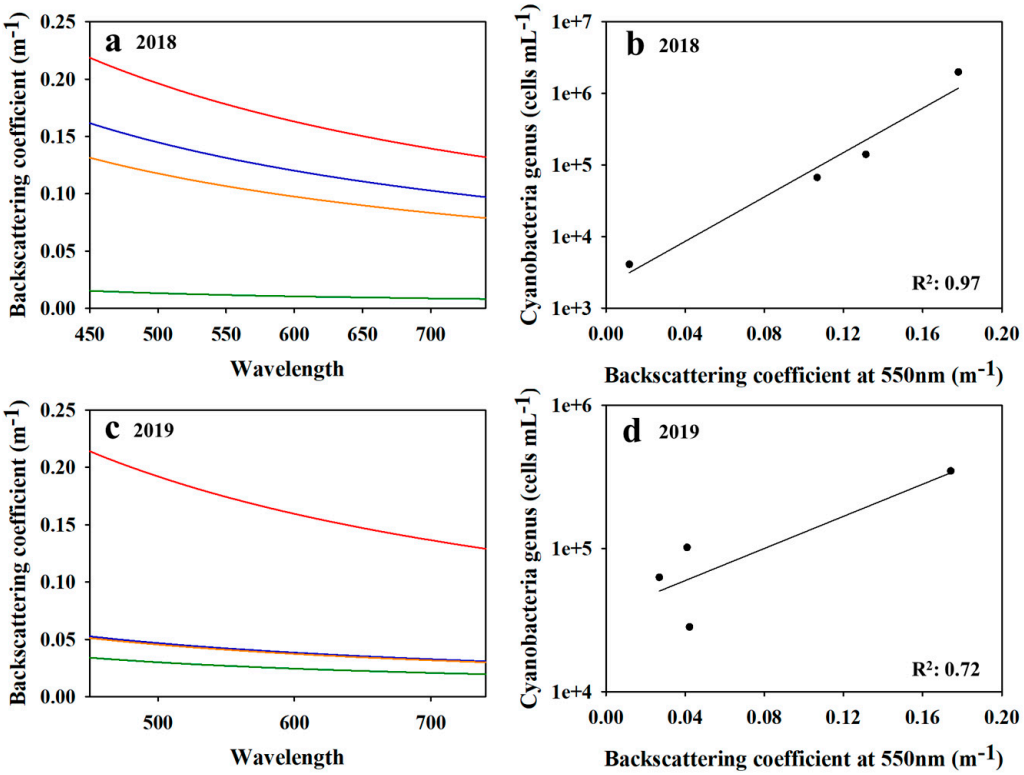

Figure 7. Backscattering coefficient spectra and the relationship between backscattering coefficient and cyanobacteria cells—(**a**) is the backscattering coefficient for 26 July 2018 (blue line), 16 August 2018 (orange line), 9 September 2018 (red line), and 25 October 2018 (green line); (**b**) is the correlation between the backscattering coefficient and cyanobacteria cells at 550 nm for 2018; (**c**) is the backscattering coefficient for 9 July 2019 (blue line), 24 July 2019 (red line), 8 August 2019 (orange line), and 18 September 2019 (green line); and (**d**) is the relationship between the backscattering coefficient and cyanobacteria cells at 550 nm.

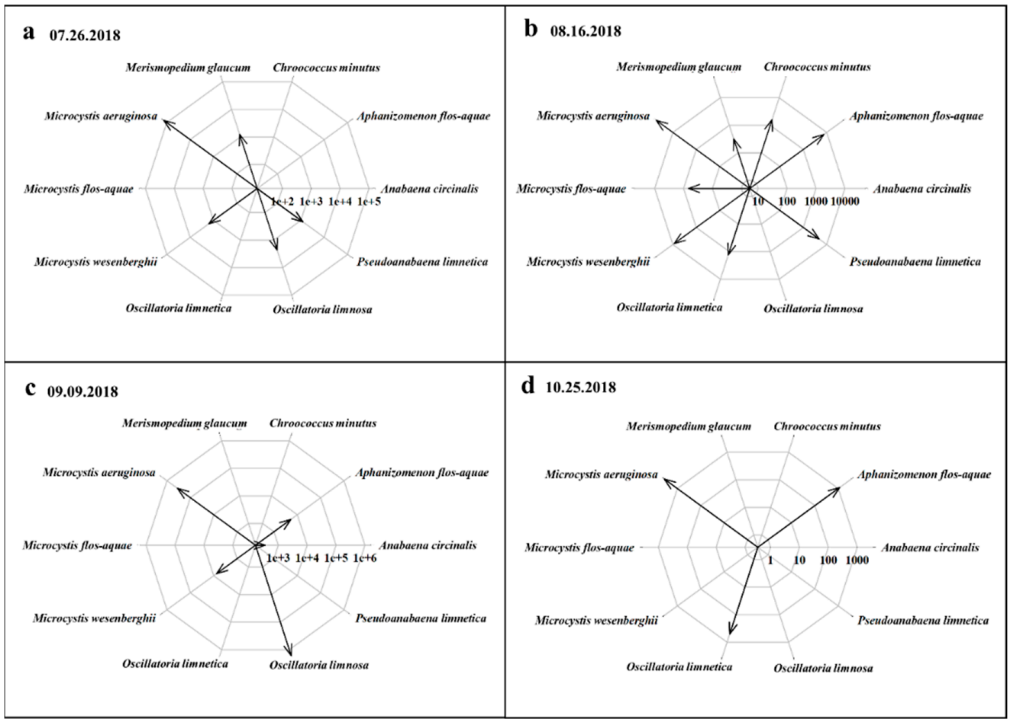

Figure 8. Radar plot of cyanobacteria cell composition with backscattering coefficient values at 550 nm for 2018—(**a**) is the cell composition on 26 July; (**b**) is the composition on 16 August; (**c**) is the composition on 9 September; and (**d**) is the composition on 25 October. The black arrow indicates the concentration of cyanobacteria genus cells; the unit of concentration is cells mL^{-1}.

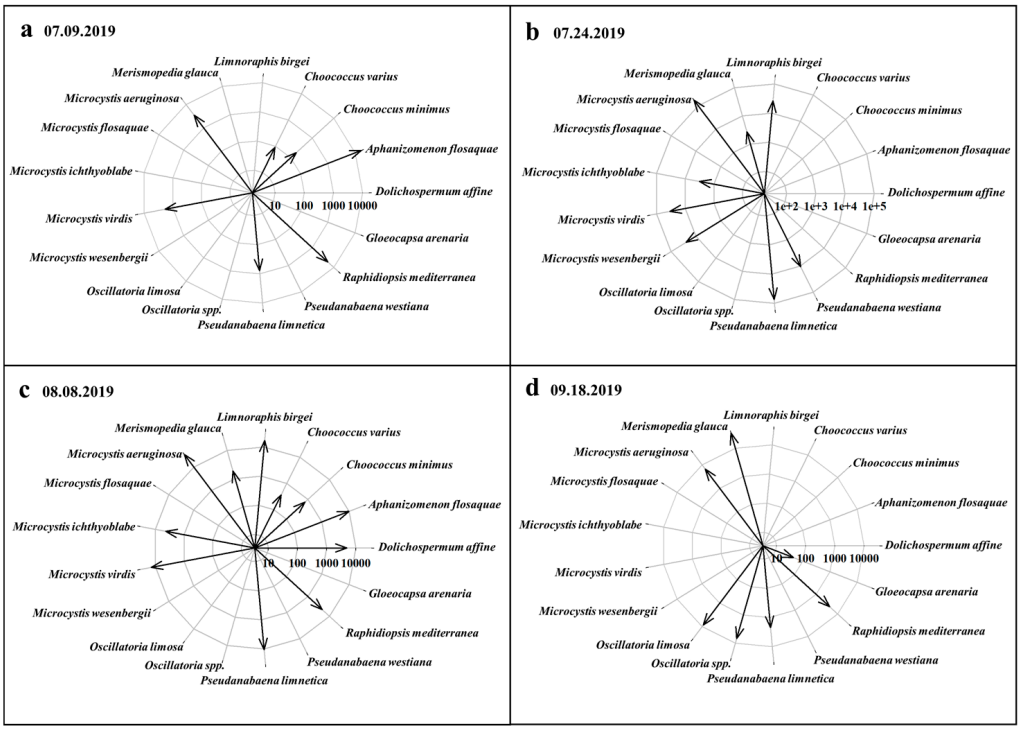

Figure 9. Radar plot of cyanobacteria cell composition with backscattering coefficient values at 550 nm for 2019—(**a**) is the cell composition on 9 July; (**b**) is the composition on 24 July 24; (**c**) is the composition on 8 August; and (**d**) is the composition on 18 September. The black arrow indicates the concentration of cyanobacteria genus cells; the unit of concentration is cells mL^{-1}.

4. Conclusions

This study developed GUI software to perform a sensitivity analysis of the parameters of the HydroLight model using multiple executions. The GUI model carried out the LH–OAT sampling of selected parameters, multi-point simulations, and sensitivity analysis; furthermore, it displayed the sensitivity analysis results. The Chl-a concentrations, TSS concentrations, and absorption coefficients for inland water in the HN and DC regions of the Daecheong dam area were measured to simulate the reflectance profiles using the model. The sensitivity analysis results showed that the scattering parameters correspond to Chl-a and TSS were more important than the other parameters. In particular, the backscattering ratios of TSS and Chl-a were the most sensitive parameters for the HN and CS regions, respectively, because TSS was a major constituent in the water in HN and Chl-a was a major constituent in that in CS. Moreover, this study calibrated the HydroLight parameters to estimate the reflectance profiles of inland water bodies. The simulated reflectance profiles showed good agreement with direct observations. In addition, the scattering property was strongly correlated with the cyanobacteria genera cells. The differences and similarities between the parameter values obtained in this study and those previously obtained based on oceanography were elucidated. It was found that the proposed GUI software extends the applicability of the HydroLight model and significantly reduces simulation time. With regard to related future work, the optical algorithm included in the GUI software can be practically applied to directly obtain information regarding the algal biomass in water bodies.

Author Contributions: Conceptualization, J.C.P., Y.S.K., and K.H.C.; methodology, J.C.P. and Y.S.K.; software, J.C.P. and Y.S.K.; validation, J.-H.A., Y.-H.K., and K.H.C.; formal analysis, J.C.P., Y.S.K., and S.-S.B.; investigation, J.C.P. and Y.S.K.; resources, J.C.P. and Y.S.K.; data curation, J.C.P. and Y.S.K.; writing—original draft preparation, J.C.P.; writing—review and editing, J.-H.A., Y.-H.K., and K.H.C.; visualization, J.C.P.; supervision, K.H.C. All authors have read and agreed to the published version of the manuscript.

Funding: This research was supported by Korea Environment Industry & Technology Institute (KEITI) through the "Aquatic Ecosystem Conservation Research Program", funded by the Korea Ministry of Environment (MOE) [No. 2020003050001] and was also supported by the ICT R&D program of MSIT/IITP (2018-0-00219, Space-time complex artificial intelligence blue-green algae prediction technology based on direct-readable water quality complex sensor and hyperspectral image).

Conflicts of Interest: The authors declare no conflict of interest.

Appendix A

Table A1. Observed Chl-a in HN and CS regions.

Chl-a	2018					2019				
Region	**Date**	**0+**	**0−**	**0.5 m**	**1.0 m**	**Date**	**0+**	**0−**	**0.5 m**	**1.0 m**
HN (n = 23)	07/27	6.99 ± 0.81	6.98 ± 0.81	7.56 ± 0.33	8.03 ± 1.21	07/09	2.86 ± 0.18	3.03 ± 0.26	3.30 ± 0.43	3.75 ± 0.54
	-	-	-	-	-	07/24	5.42 ± 0.93	5.47 ± 0.99	6.03 ± 0.56	6.62 ± 0.55
	-	-	-	-	-	08/24	6.08 ± 0.43	6.08 ± 0.43	6.07 ± 0.44	6.05 ± 0.40
	-	-	-	-	-	09/18	2.48 ± 0.44	2.40 ± 0.56	3.58 ± 0.47	5.19 ± 0.67
CS (n = 104)	07/27	10.77 ± 3.52	11.78 ± 3.89	14.20 ± 3.66	17.20 ± 3.03	07/09	12.47 ± 1.42	12.93 ± 1.53	14.58 ± 2.22	15.71 ± 2.25
	08/16	7.95 ± 2.31	8.07 ± 2.31	8.50 ± 1.65	7.99 ± 1.17	07/24	15.51 ± 4.94	15.57 ± 4.90	11.65 ± 3.39	9.10 ± 3.15
	09/06	17.52 ± 12.81	16.07 ± 12.56	8.93 ± 7.83	5.13 ± 4.33	08/08	7.33 ± 1.56	7.33 ± 1.56	8.17 ± 1.93	7.70 ± 0.83
	09/17	4.59 ± 1.36	5.01 ± 1.21	10.06 ± 9.27	8.23 ± 3.50	08/23	7.69 ± 0.88	7.69 ± 0.88	7.63 ± 0.79	7.09 ± 0.85
	09/19	8.37 ± 3.82	8.86 ± 3.15	9.00 ± 2.08	6.92 ± 1.52	09/17	5.25 ± 1.26	6.24 ± 1.10	9.50 ± 3.35	12.51 ± 3.61
	10/11	10.17 ± 1.33	9.11 ± 1.61	7.69 ± 1.56	7.69 ± 1.56	-	-	-	-	-
	10/25	5.53 ± 2.44	5.57 ± 2.44	9.54 ± 2.89	12.00 ± 1.67	-	-	-	-	-

n is number of samples, and 0+ and 0- indicate the concentrations at the surface and beneath the surface of water, respectively.

Table A2. Observed TSS in HN and CS region.

TSS		2018					2019			
Region	**Date**	**0+**	**0−**	**0.5 m**	**1.0 m**	**Date**	**0+**	**0−**	**0.5 m**	**1.0 m**
HN (n = 23)	07/27	5.43 ± 1.30	5.09 ± 0.77	4.90 ± 0.58	4.78 ± 0.55	07/09	4.31 ± 0.11	4.42 ± 0.17	4.59 ± 0.28	4.88 ± 0.35
	-	-	-	-	-	07/24	6.22 ± 0.33	6.22 ± 0.35	6.36 ± 0.36	6.75 ± 0.36
	-	-	-	-	-	08/24	6.34 ± 0.26	6.34 ± 0.26	6.39 ± 0.29	6.38 ± 0.26
	-	-	-	-	-	09/18	3.88 ± 0.22	4.01 ± 0.37	4.77 ± 0.31	5.82 ± 0.43
CS (n = 104)	07/27	9.16 ± 2.01	9.64 ± 1.89	9.39 ± 1.97	9.10 ± 1.80	07/09	11.05 ± 1.12	11.42 ± 1.21	12.72 ± 1.75	13.61 ± 1.78
	08/16	14.83 ± 6.34	14.56 ± 6.31	14.22 ± 6.10	13.66 ± 4.85	07/24	13.45 ± 3.90	13.50 ± 3.87	10.40 ± 2.68	8.39 ± 2.49
	09/06	12.90 ± 2.36	12.98 ± 2.30	12.57 ± 1.98	12.85 ± 2.30	08/08	7.00 ± 1.23	7.00 ± 1.23	7.65 ± 1.53	7.29 ± 0.66
	09/17	10.73 ± 1.77	10.92 ± 2.20	11.44 ± 3.59	11.33 ± 2.77	08/23	7.28 ± 0.75	7.28 ± 0.75	7.23 ± 0.68	6.81 ± 0.72
	09/19	13.24 ± 3.81	13.13 ± 3.81	13.57 ± 3.11	12.39 ± 3.11	09/17	5.35 ± 1.00	6.13 ± 0.87	8.71 ± 2.64	11.09 ± 2.85
	10/11	4.60 ± 1.39	4.60 ± 1.39	2.93 ± 0.48	2.97 ± 0.52	-	-	-	-	-
	10/25	5.29 ± 2.57	5.29 ± 2.57	9.84 ± 2.71	12.42 ± 1.60	-	-	-	-	-

n is the number of samples, and 0+ and 0- indicate the concentrations at the surface and beneath the surface of the water, respectively.

References

1. Ho, J.C.; Stumpf, R.P.; Bridgeman, T.B.; Michalak, A.M. Using Landsat to Extend the Historical Record of Lacustrine Phytoplankton Blooms: A Lake Erie Case Study. *Remote Sens. Environ.* **2017**, *191*, 273–285. [CrossRef]
2. Karki, S.; Sultan, M.; Elkadiri, R.; Elbayoumi, T. Mapping and Forecasting Onsets of Harmful Algal Blooms Using MODIS Data over Coastal Waters Surrounding Charlotte County, Florida. *Remote Sens.* **2018**, *10*, 1656.
3. Smith, M.E.; Bernard, S. Satellite Ocean Color Based Harmful Algal Bloom Indicators for Aquaculture Decision Support in the Southern Benguela. *Front. Mar. Sci.* **2020**, *7*, 1–13. [CrossRef]
4. Cullen, J.J.; Ciotti, A.M.; Davis, R.F.; Lewis, M.R. Optical Detection and Assessment of Algal Blooms. *Limnol. Oceanogr.* **1997**, *42*, 1223–1239. [CrossRef]
5. Roesler, C.S.; Perry, M.J. In Situ Phytoplankton Absorption, Fluorescence Emission, and Particulate Backscattering Spectra Determined from Reflectance. *J. Geophys. Res. Oceans* **1995**, *100*, 13279–13294. [CrossRef]
6. Kutser, T.; Metsamaa, L.; Dekker, A.G. Influence of the Vertical Distribution of Cyanobacteria in the Water Column on the Remote Sensing Signal. *Estuar. Coast. Shelf Sci.* **2008**, *78*, 649–654.
7. Mobley, C.D. Estimation of the Remote-Sensing Reflectance from Above-Surface Measurements. *Appl. Opt.* **1999**, *38*, 7442–7455. [CrossRef] [PubMed]
8. Craig, S.E.; Lohrenz, S.E.; Lee, Z.; Mahoney, K.L.; Kirkpatrick, G.J.; Schofield, O.M.; Steward, R.G. Use of Hyperspectral Remote Sensing Reflectance for Detection and Assessment of the Harmful Alga, Karenia Brevis. *Appl. Opt.* **2006**, *45*, 5414–5425. [CrossRef]
9. Wang, J.; Cota, G.F. Remote-Sensing Reflectance in the Beaufort and Chukchi Seas: Observations and Models. *Appl. Opt.* **2003**, *42*, 2754–2765. [CrossRef]
10. Stramska, M.; Stramski, D. Effects of a Nonuniform Vertical Profile of Chlorophyll Concentration on Remote-Sensing Reflectance of the Ocean. *Appl. Opt.* **2005**, *44*, 1735–1747. [CrossRef]
11. Xue, K.; Zhang, Y.; Ma, R.; Duan, H. An Approach to Correct the Effects of Phytoplankton Vertical Nonuniform Distribution on Remote Sensing Reflectance of Cyanobacterial Bloom Waters. *Limnol. Oceanogr. Methods* **2017**, *15*, 302–319. [CrossRef]
12. Golladay, S.W.; Sinsabaugh, R.L. Biofilm Development on Leaf and Wood Surfaces in a Boreal River. *Freshw. Biol.* **1991**, *25*, 437–450. [CrossRef]
13. Moore, T.S.; Churnside, J.H.; Sullivan, J.M.; Twardowski, M.S.; Nayak, A.R.; McFarland, M.N.; Nicole, D.S.; Richard, W.G.; Thomas, H.J.; Ruberg, S.A. Vertical Distributions of Blooming Cyanobacteria Populations in a Freshwater Lake from LIDAR Observations. *Remote Sens. Environ.* **2019**, *225*, 347–367. [CrossRef]
14. Jensen, D.; Simard, M.; Cavanaugh, K.; Sheng, Y.; Fichot, C.G.; Pavelsky, T.; Twilley, R. Improving the Transferability of Suspended Solid Estimation in Wetland and Deltaic Waters with an Empirical Hyperspectral Approach. *Remote Sens.* **2019**, *11*, 1629. [CrossRef]
15. Kwon, Y.S.; Pyo, J.; Kwon, Y.H.; Duan, H.; Cho, K.H.; Park, Y. Drone-Based Hyperspectral Remote Sensing of Cyanobacteria Using Vertical Cumulative Pigment Concentration in a Deep Reservoir. *Remote Sens. Environ.* **2020**, *236*, 111517. [CrossRef]
16. Mishra, S.; Mishra, D.R. Normalized Difference Chlorophyll Index: A Novel Model for Remote Estimation of Chlorophyll-A Concentration in Turbid Productive Waters. *Remote Sens. Environ.* **2012**, *117*, 394–406. [CrossRef]
17. Tan, J.; Cherkauer, K.A.; Chaubey, I.; Troy, C.D.; Essig, R. Water Quality Estimation of River Plumes in Southern Lake Michigan Using Hyperion. *J. Great Lakes Res.* **2016**, *42*, 524–535.
18. Hamby, D.M. A Review of Techniques for Parameter Sensitivity Analysis of Environmental Models. *Environ. Monit. Assess.* **1994**, *32*, 135–154. [CrossRef] [PubMed]
19. Pianosi, F.; Beven, K.; Freer, J.; Hall, J.W.; Rougier, J.; Stephenson, D.B.; Wagener, T. Sensitivity Analysis of Environmental Models: A Systematic Review with Practical Workflow. *Environ. Model. Softw.* **2016**, *79*, 214–232. [CrossRef]
20. Bukata, R.P.; Jerome, J.H.; Kondratyev, K.Y.; Pozdnyakov, D.V. Satellite Monitoring of Optically-Active Components of Inland Waters: An Essential Input to Regional Climate Change Impact Studies. *J. Great Lakes Res.* **1991**, *17*, 470–478. [CrossRef]
21. Helton, J.C.; Iman, R.L.; Brown, J.B. Sensitivity Analysis of the Asymptotic Behavior of a Model for the Environmental Movement of Radionuclides. *Ecol. Model.* **1985**, *28*, 243–278. [CrossRef]

22. Park, H.S.; Yoon, S.W.; Chung, S.W.; Hwang, H.S. Effect of Pollutants Control Measures in So-Oak Watershed on the Control of Algae Growth in Daecheong Reservoir. *J. Environ. Impact Assess.* **2016**, *25*, 248–260. [CrossRef]
23. Lee, J.J.; Yoon, J.; Choi, I.; Joo, H.; Lim, B.; Lee, S. Vertical Distribution of Harmful Cyanobacterial in the Daechung Reservoir. *J. Korean Soc. Water Environ.* **2016**, *1*, 464–465.
24. Pyo, J.; Ha, S.; Pachepsky, Y.A.; Lee, H.; Ha, R.; Nam, G.; Kim, M.S.; Im, J.; Cho, K.H. Chlorophyll-A Concentration Estimation Using Three Difference Bio-Optical Algorithms, Including a Correction for the Low-Concentration Range: The Case of the Yiam Reservoir, Korea. *Remote Sens. Lett.* **2016**, *7*, 407–416. [CrossRef]
25. Ministry of Environment (MOE). *Standard Methods for Examination of Water Pollution*; Ministry of Environment (MOE): Seoul, Korea, 2020.
26. Mobley, C.D.; Sundman, L.K. *HydroLight 5.2 User's Guide*; Sequoia Scientific: Washington, DC, USA, 2013.
27. Gordon, H.R.; Morel, A. Remote Assessment of Ocean Color for Interpretation of Satellite Visible Imagery. A Review. In *Lecture Notes on Coastal and Estuarine Studies*; Springcr-Vcrlag: New York, NY, USA, 1983; p. 114.
28. McKay, J. *Sensitivity and Uncertainty Analysis Using a Statistical Sample of Input Values Uncertainty Analysis*; Ronen, Y., Ed.; CRC Press: Boca Raton, FL, USA, 1988.
29. Campolongo, F.; Saltelli, A.; Cariboni, J. From Screening to Quantitative Sensitivity Analysis. A Unified Approach. *Comput. Phys. Commun.* **2011**, *182*, 978–988. [CrossRef]
30. Morris, M.D. Factorial Sampling Plans for Preliminary Computational Experiments. *Technometrics* **1991**, *33*, 161–174. [CrossRef]
31. Cho, K.H.; Pachepsky, Y.; Kim, J.H.; Guber, A.; Shelton, D.; Rowland, R. Release of Escherichia coli from the Bottom Sediment in a First-Order Creek: Experiment and Reach-Specific Modeling. *J. Hydrol.* **2010**, *391*, 322–332.
32. van Griensven, A.; Meixner, T.; Grunwald, S.; Bishop, T.; Diluzio, M.; Srinivasan, R. A Global Sensitivity Analysis Tool for the Parameters of Multi-Variable Catchment Models. *J. Hydrol.* **2006**, *324*, 10–23. [CrossRef]
33. Saltelli, A.; Ratto, M.; Andres, T.; Campolongo, F.; Cariboni, J.; Gatelli, D.; Saisana, M.; Tarantola, S. *Global Sensitivity Analysis: The Primer*; John Wiley & Sons: Hoboken, NJ, USA, 2008.
34. Sin, G.; Gernaey, K.V. Improving the Morris Method for Sensitivity Analysis by Scaling the Elementary Effects. *Comput. Aided Chem. Eng.* **2009**, *26*, 925–930.
35. Campolongo, F.; Braddock, R. The Use of Graph Theory in the Sensitivity Analysis of the Model Output: A Second Order Screening Method. *Reliab. Eng. Syst. Saf.* **1999**, *64*, 1–12. [CrossRef]
36. Pianosi, F.; Sarrazin, F.; Wagener, T. A Matlab Toolbox for Global Sensitivity Analysis. *Environ. Model. Softw.* **2015**, *70*, 80–85. [CrossRef]
37. Torczon, V. On the Convergence of the Multidirectional Search Algorithm. *SIAM J. Optim.* **1991**, *1*, 123–145. [CrossRef]
38. van Vliet, J.; Bregt, A.K.; Brown, D.G.; van Delden, H.; Heckbert, S.; Verburg, P.H. A Review of Current Calibration and Validation Practices in Land-Change Modeling. *Environ. Model. Softw.* **2016**, *82*, 174–182. [CrossRef]
39. Sun, D.; Li, Y.; Wang, Q.; Lv, H.; Le, C.; Huang, C.; Gong, S. Partitioning Particulate Scattering and Absorption into Contributions of Phytoplankton and Non-Algal Particles in Winter in Lake Taihu (China). *Hydrobiologia* **2010**, *644*, 337–349. [CrossRef]
40. Gibson, R.N.; Atkinson, R.J.A.; Gordon, J.D. *Oceanography and Marine Biology: An Annual Review*; CRC Press: Boca Raton, FL, USA, 2007.
41. Keck, T.; Preusker, R.; Fischer, J. Estimating Chlorophyll-A Absorption with the Total Algae Peak Integration Retrieval TAPIR Considering Chlorophyll-A Fluorescence from Hyperspectral Top of the Atmosphere Signals in Optically Complex Waters. *Preprints* **2018**, *1*, 1–18. [CrossRef]
42. Twardowski, M.S.; Boss, E.; Sullivan, J.M.; Donaghay, P.L. Modeling the Spectral Shape of Absorption by Chromophoric Dissolved Organic Matter. *Mar. Chem.* **2004**, *89*, 69–88. [CrossRef]
43. Lyu, H.; Wang, Q.; Wu, C.; Zhu, L.; Li, Y.; Huang, J. Variations in Optical Scattering and Backscattering by Organic and Inorganic Particulates in Chinese Lakes of Taihu, Chaohu and Dianchi. *Chin. Geogr. Sci.* **2015**, *25*, 26–38.
44. Bartlett, J.S.; Voss, K.J.; Sathyendranath, S.; Vodacek, A. Raman Scattering by Pure Water and Seawater. *Appl. Opt.* **1988**, *37*, 3324–3332. [CrossRef]
45. Bowling, L.C.; Zamyadi, A.; Henderson, R.K. Assessment of In Situ Fluorometry to Measure Cyanobacterial Presence in Water Bodies with Diverse Cyanobacterial Populations. *Water Res.* **2016**, *105*, 22–33. [CrossRef]
46. Chaffin, J.D.; Kane, D.D.; Stanislawczyk, K.; Parker, E.M. Accuracy of Data Buoys for Measurement of Cyanobacteria, Chlorophyll, and Turbidity in a Large Lake (Lake Erie, North America): Implications for Estimation of Cyanobacterial Bloom Parameters from Water Quality Sonde Measurements. *Environ. Sci. Pollut. Res.* **2018**, *25*, 25175–25189. [CrossRef]
47. Choo, F.; Zamyadi, A.; Stuetz, R.M.; Newcombe, G.; Newton, K.; Henderson, R.K. Enhanced Real-Time Cyanobacterial Fluorescence Monitoring through Chlorophyll-A Interference Compensation Corrections. *Water Res.* **2019**, *148*, 86–96. [CrossRef]
48. Zolfaghari, K.; Wilkes, G.; Bird, S.; Ellis, D.; Pintar, K.D.M.; Gottschall, N.; McNairn, H.; Lapen, D.R. Chlorophyll-A, Dissolved Organic Carbon, Turbidity and Other Variables of Ecological Importance in River Basins in Southern Ontario and British Columbia, Canada. *Environ. Monit. Assess.* **2020**, *192*, 1–16. [CrossRef] [PubMed]
49. Walsby, A.E.; Booker, M.J. Changes in Buoyancy of a Planktonic Blue-Green Alga in Response to Light Intensity. *Br. Phycol. J.* **1980**, *15*, 311–319. [CrossRef]
50. Modenutti, B.; Pérez, G.; Balseiro, E.; Queimaliños, C. The Relationship between Light Attenuation, Chlorophyll A and Total Suspended Solids in a Southern Andes Glacial Lake. *Int. Ver. Theor. Angew. Limnol. Verh.* **2000**, *27*, 2648–2651. [CrossRef]

51. Mobley, C.D.; Sundman, L.K.; Boss, E. Phase Function Effects on Oceanic Light Fields. *Appl. Opt.* **2002**, *41*, 1035–1050. [CrossRef]
52. Twardowski, M.S.; Boss, E.; Macdonald, J.B.; Pegau, W.S.; Barnard, A.H.; Zaneveld, J.R.V. A Model for Estimating Bulk Refractive Index from the Optical Backscattering Ratio and the Implications for Understanding Particle Composition in Case I and Case II Waters. *J. Geophys. Res. Oceans* **2001**, *106*, 14129–14142.
53. Aas, E. Refractive Index of Phytoplankton Derived from Its Metabolite Composition. *J. Plankton Res.* **1996**, *18*, 2223–2249. [CrossRef]
54. Whitmire, A.L.; Boss, E.; Cowles, T.J.; Pegau, W.S. Spectral Variability of the Particulate Backscattering Ratio. *Opt. Express* **2007**, *15*, 7019–7031. [CrossRef]
55. Kutser, T.; Paavel, B.; Verpoorter, C.; Ligi, M.; Soomets, T.; Toming, K.; Casal, G. Remote Sensing of Black Lakes and Using 810 nm Reflectance Peak for Retrieving Water Quality Parameters of Optically Complex Waters. *Remote Sens.* **2016**, *8*, 497.
56. Carder, K.L.; Chen, F.R.; Lee, Z.P.; Hawes, S.; Kamykowski, D. Semi-Analytic MODIS Algorithms for Chlorophyll A and Absorption with Bio-Optical Domains Based on Nitrate-Depletion Temperatures. *J. Geophys. Res.* **1999**, *104*, 5403–5421. [CrossRef]
57. Schwarz, J.N.; Kowalczuk, P.; Kaczmarek, S.; Cota, G.F.; Mitchell, B.G.; Kahru, M.; Chavez, F.P.; Cunningham, A.; McKee, D.; Gege, P.; et al. Two Models for Absorption by Coloured Dissolved Organic Matter (CDOM). *Oceanologia* **2002**, *44*, 209–241.
58. Song, K.; Liu, D.; Li, L.; Wang, Z.; Wang, Y.; Jiang, G. Spectral Absorption Properties of Colored Dissolved Organic Matter (CDOM) and Total Suspended Matter (TSM) of Inland Waters. In *Atmospheric and Environmental Remote Sensing Data Processing and Utilization VI: Readiness for GEOSS IV*; International Society for Optics and Photonics: San Diego, CA, USA, 2010; Volume 7811, pp. 1–13.
59. Lu, Y.; Li, L.; Hu, C.; Li, L.; Zhang, M.; Sun, S.; Lv, C. Sunlight Induced Chlorophyll Fluorescence in the Near-Infrared Spectral Region in Natural Waters: Interpretation of the Narrow Reflectance Peak Around 761 nm. *J. Geophys. Res. Oceans* **2016**, *121*, 5017–5029. [CrossRef]
60. Shi, K.; Li, Y.; Li, L.; Lu, H.; Song, K.; Liu, Z.; Xu, Y.; Li, Z. Remote Chlorophyll-A Estimates for Inland Waters Based on a Cluster-Based Classification. *Sci. Total Environ.* **2013**, *444*, 1–15. [CrossRef] [PubMed]
61. Gilerson, A.; Zhou, J.; Hlaing, S.; Ioannou, I.; Gross, B.; Moshary, F.; Ahmed, S. Fluorescence Component in the Reflectance Spectra from Coastal Waters. II. Performance of Retrieval Algorithms. *Opt. Express* **2008**, *16*, 2446–2460. [CrossRef]
62. Gilerson, A.; Zhou, J.; Hlaing, S.; Ioannou, I.; Schalles, J.; Gross, B.; Moshary, F.; Ahmed, S. Fluorescence Component in the Reflectance Spectra from Coastal Waters. Dependence on Water Composition. *Opt. Express* **2007**, *15*, 15702–15721. [CrossRef] [PubMed]
63. Gordon, H.R.; McCluney, W.R. Estimation of the Depth of Sunlight Penetration in the Sea for Remote Sensing. *Appl. Opt.* **1975**, *14*, 413–416. [CrossRef]
64. Zhang, Y.; Qin, B.; Zhu, G.; Gao, G.; Luo, L.; Chen, W. Effect of Sediment Resuspension on Underwater Light Field in Shallow Lakes in the Middle and Lower Reaches of the Yangtze River: A Case Study in Longgan Lake and Taihu Lake. *Sci. China Ser. D* **2006**, *49*, 114–125. [CrossRef]
65. Shen, M.; Duan, H.; Cao, Z.; Xue, K.; Loiselle, S.; Yesou, H. Determination of the Downwelling Diffuse Attenuation Coefficient of Lake Water with the Sentinel-3A OLCI. *Remote Sens.* **2017**, *9*, 1246. [CrossRef]
66. Lee, Z.; Carder, K.L.; Du, K. Effects of Molecular and Particle Scatterings on the Model Parameter for Remote-Sensing Reflectance. *Appl. Opt.* **2004**, *43*, 4957–4964.
67. Nouchi, V.; Odermatt, D.; Wüest, A.; Bouffard, D. Effects of Non-Uniform Vertical Constituent Profiles on Remote Sensing Reflectance of Oligo-to Mesotrophic Lakes. *Eur. J. Remote Sens.* **2018**, *51*, 808–821. [CrossRef]
68. Loisel, H.; Mériaux, X.; Berthon, J.F.; Poteau, A. Investigation of the Optical Backscattering to Scattering Ratio of Marine Particles in Relation to Their Biogeochemical Composition in the Eastern English Channel and Southern North Sea. *Limnol. Oceanogr.* **2007**, *52*, 739–752. [CrossRef]
69. Snyder, W.A.; Arnone, R.A.; Davis, C.O.; Goode, W.; Gould, R.W.; Ladner, S.; Lamela, G.; Rhea, W.J.; Stavn, R.; Sydor, M.; et al. Optical Scattering and Backscattering by Organic and Inorganic Particulates in US Coastal Waters. *Appl. Opt.* **2008**, *47*, 666–677. [CrossRef]
70. Xi, H.; Larouche, P.; Michel, C.; Tang, S. Beam Attenuation, Scattering and Backscattering of Marine Particles in Relation to Particle Size Distribution and Composition in Hudson Bay (Canada). *J. Geophys. Res. Oceans* **2015**, *120*, 3286–3300. [CrossRef]
71. McKee, D.; Chami, M.; Brown, I.; Calzado, V.S.; Doxaran, D.; Cunningham, A. Role of Measurement Uncertainties in Observed Variability in the Spectral Backscattering Ratio: A Case Study in Mineral—Rich Coastal Waters. *Appl. Opt.* **2009**, *48*, 4663–4675. [CrossRef]
72. Organelli, E.; Dall'Olmo, G.; Brewin, R.J.; Tarran, G.A.; Boss, E.; Bricaud, A. The Open-Ocean Missing Backscattering is in the Structural Complexity of Particles. *Nat. Commun.* **2018**, *9*, 1–11. [CrossRef]
73. Ulloa, O.; Sathyendranath, S.; Platt, T. Effect of the Particle-Size Distribution on the Backscattering Ratio in Seawater. *Appl. Opt.* **1994**, *33*, 7070–7077. [CrossRef]
74. McKee, D.; Cunningham, A. Identification and Characterisation of Two Optical Water Types in the Irish Sea from in Situ Inherent Optical Properties and Seawater Constituents. *Estuar. Coast. Shelf Sci.* **2006**, *68*, 305–316. [CrossRef]
75. Boss, E.; Pegau, W.S.; Lee, M.; Twardowski, M.; Shybanov, E.; Korotaev, G.; Baratange, F. Particulate Backscattering Ratio at LEO 15 and Its Use to Study Particle Composition and Distribution. *J. Geophys. Res. Oceans* **2004**, *109*, 1–10. [CrossRef]

76. Haltrin, V.I.; Lee, M.; Shybanov, E.; Arnone, R.A.; Weidemann, A.D. *Relationship between Backscattering and Beam Scattering Coefficients Derived from New Measurements of Light Scattering Phase Functions*; Naval Research Lab Stennis Space Center: Hancock County, MS, USA, 2002.
77. Arst, H.; Arst, K.I.; Arst, K.I. *Optical Properties and Remote Sensing of Multicomponental Water Bodies*; Springer Science & Business Media: Berlin/Heidelberg, Germany, 2003.
78. Stramski, D.; Kiefer, D.A. Light Scattering by Microorganisms in the Open Ocean. *Prog. Oceanogr.* **1991**, *28*, 343–383.
79. Green, S.A.; Blough, N.V. Optical Absorption and Fluorescence Properties of Chromophoric Dissolved Organic Matter in Natural Waters. *Limnol. Oceanogr.* **1994**, *39*, 1903–1916. [CrossRef]
80. Stedmon, C.A.; Markager, S. The Optics of Chromophoric Dissolved Organic Matter (CDOM) in the Greenland Sea: An Algorithm for Differentiation between Marine and Terrestrially Derived Organic Matter. *Limnol. Oceanogr.* **2001**, *46*, 2087–2093. [CrossRef]
81. Feng, C.; Ishizaka, J.; Saitoh, K.; Mine, T.; Yamashita, H. A Novel Method Based on Backscattering for Discriminating Summer Blooms of the Raphidophyte (Chattonella spp.) and the Diatom (Skeletonema spp.) using MODIS Images in Ariake Sea, Japan. *Remote Sens.* **2020**, *12*, 1504. [CrossRef]
82. Ostrovsky, I.; Wu, S.; Li, L.; Song, L. Bloom-Forming Toxic Cyanobacterium Microcystis: Quantification and Monitoring with a High-Frequency Echosounder. *Water Res.* **2020**, *183*, 116091. [CrossRef]
83. Subramaniam, A.; Carpenter, E.J.; Karentz, D.; Falkowski, P.G. Bio-Optical Properties of the Marine Diazotrophic Cyanobacteria Trichodesmium spp. I. Absorption and Photosynthetic Action Spectra. *Limnol. Oceanogr.* **1999**, *44*, 608–617. [CrossRef]
84. Simis, S.G.; Ruiz-Verdú, A.; Domínguez-Gómez, J.A.; Peña-Martinez, R.; Peters, S.W.; Gons, H.J. Influence of Phytoplankton Pigment Composition on Remote Sensing of Cyanobacterial Biomass. *Remote Sens. Environ.* **2007**, *106*, 414–427. [CrossRef]
85. Dupouy, C.; Neveux, J.; Dirberg, G.; Rottgers, R.; Tenório, M.M.B.; Ouillon, S. Bio-Optical Properties of the Marine Cyanobacteria Trichodesmium spp. *J. Appl. Remote Sens.* **2008**, *2*, 023503.
86. Volten, H.; De Haan, J.F.; Hovenier, J.W.; Schreurs, R.; Vassen, W.; Dekker, A.G.; Hoogenboom, H.J.; Charlton, F.; Wouts, R. Laboratory Measurements of Angular Distributions of Light Scattered by Phytoplankton and Silt. *Limnol. Oceanogr.* **1998**, *43*, 1180–1197. [CrossRef]
87. Matthews, M.W.; Bernard, S.; Winter, K. Remote Sensing of Cyanobacteria-Dominant Algal Blooms and Water Quality Parameters in Zeekoevlei, A Small Hypertrophic Lake, Using MERIS. *Remote Sens. Environ.* **2010**, *114*, 2070–2087. [CrossRef]
88. Kudela, R.M.; Palacios, S.L.; Austerberry, D.C.; Accorsi, E.K.; Guild, L.S.; Torres-Perez, J. Application of Hyperspectral Remote Sensing to Cyanobacterial Blooms in Inland Waters. *Remote Sens. Environ.* **2015**, *167*, 196–205. [CrossRef]
89. Jansson, P.E.; Moon, D.S. A Coupled Model of Water, Heat and Mass Transfer Using Object Orientation to Improve Flexibility and Functionality. *Environ. Model. Softw.* **2001**, *16*, 37–46. [CrossRef]
90. Refsgaard, J.C.; van der Sluijs, J.P.; Højberg, A.L.; Vanrolleghem, P.A. Uncertainty in the Environmental Modelling Process—A Framework and Guidance. *Environ. Model. Softw.* **2007**, *22*, 1543–1556. [CrossRef]
91. Smith, S.T. *MATLAB: Advanced GUI Development*; Dog Ear Publishing: Indianapolis, IN, USA, 2006.
92. Zhai, Z.; Cheng, B.; Wang, Z.; Liu, X.; Liu, M.; Chen, J. Design and Implementation: The End User Development Ecosystem for Cross-Platform Mobile Applications. In Proceedings of the 25th International Conference Companion on World Wide Web, Geneva, Switzerland, 11–15 April 2016; pp. 143–144.